

## **Petrography, Geochemistry, Tectonic-Magmatic Setting, and Petrogenesis of Gabbroic Rocks in the Robot-Shahr Babak Area, Kerman, Iran**

Sheida Akmal<sup>\*</sup>, Abbas Moradian<sup>a</sup>, Hamid Ahmadipour<sup>b</sup>, Massimo Tiepolo<sup>c</sup>

<sup>\*</sup>Department of Geology, Shahid Bahonar University, Kerman, Iran. [Sheidaakmali65@gmail.com](mailto:Sheidaakmali65@gmail.com)

<sup>a</sup>Department of Geology, Shahid Bahonar University, Kerman, Iran. [moradian@uk.ac.ir](mailto:moradian@uk.ac.ir)

<sup>b</sup>Department of Geology, Shahid Bahonar University, Kerman, Iran. [hahmadi@uk.ac.ir](mailto:hahmadi@uk.ac.ir)

<sup>c</sup>Department of Earth Sciences, Università Degli Studi Di Milano, Italy. [Massimo.Tiepolo@unimi.it](mailto:Massimo.Tiepolo@unimi.it)

### **Abstract:**

The study area is located in the southeastern part of the Sanandaj-Sirjan Zone (SSZ). The rock unit outcrops include olivine gabbro, troctolite, dunite, and granodiorite. In this area, the gabbro bodies are arranged separately but close to each other in two rows along the northern margin of the Shahr-Babak granodiorite batholith, which dates back to the Jurassic. This granodiorite body consists of multiple phases, with the oldest phase being Jurassic in age. The final magmatic phase is represented by a granodiorite body of Eocene age, which outcrops among the gabbros. On a microscopic scale, the plagioclase and pyroxenes in the samples from this region exhibit sieve texture and zoning, indicating disequilibrium conditions during magma solidification. These textures are attributed to the presence of hydrous minerals and changes in water fugacity. The chemical composition of the samples collected from the study area exhibits a sub-alkaline (tholeiitic to calc-alkaline) signature, ranging from gabbro to peridotite-gabbro. These rocks are related to subduction and occur in a continental arc. Additionally, they have been contaminated by material from the upper continental crust. The parent magma of the samples in this area originated from an enriched spinel-lherzolite mantle.

**Keywords:** Gabbro, Subduction, Sanandaj-Sirjan Zone (SSZ), Robat, Shahr-Babak, Kerman.

## Introduction

The geology of Iran is one of the world's prime examples of continent-continent collision. The ongoing convergence between the Arabian and Eurasian plates has led to the formation of the Zagros orogeny (Morley et al., 2009). The Zagros orogenic belt extends 1500 km from the Turkey-Iran border in the northwest, stretching from western Iran to the Persian Gulf in the southeast. This belt is divided into three parallel structural units: the Zagros Fold-Thrust Belt (ZFTB), the Sanandaj-Sirjan Zone (SSZ), and the Urumieh-Dokhtar Magmatic Arc (UDMA) (Berberian and King, 1981; Alavi, 1994).

The study area is located between longitudes  $54^{\circ} 34'$  to  $54^{\circ} 43'$  and latitudes  $29^{\circ} 56'$  to  $29^{\circ} 58'$ , in the southeastern part of the Sanandaj-Sirjan magmatic-metamorphic zone. Additionally, the area is situated approximately 31 kilometers southwest of Shahr-Babak city, to the north of the Shahr-Babak granodiorite batholith. The locations of Kerman, Shahr-Babak, and the study area are shown on the modified geology map from the Geological Survey of Iran, based on the reports of Berberian and King, 1981; Alavi, 1991; Mohajjel et al., 2003; Azizi and Moinevaziri, 2009 (Fig 1). Also, the position of this area is exhibited on the 1:250000 Neyriz geological map from the Geological Survey of Iran (Valeh and Alavi Tehrani, 1985) (Fig 2).

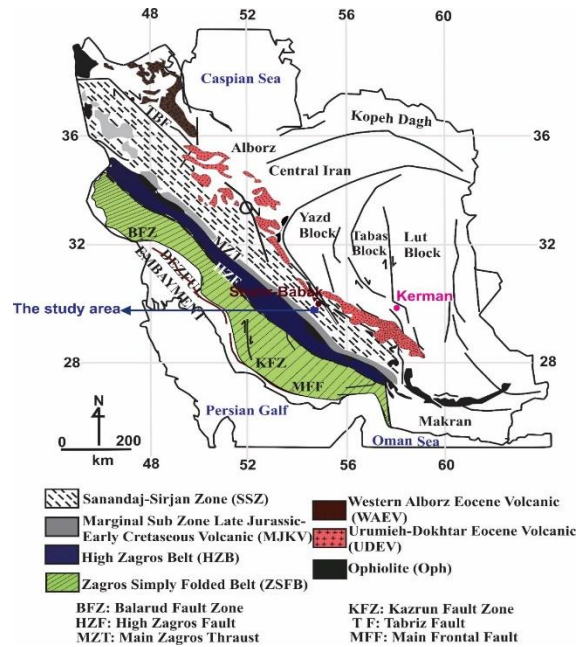


Fig 1. The locations of Kerman, Shahr-Babak, and the study area of Robot are shown on the modified geological map of the Geological Survey of Iran (Berberian and King, 1981; Alavi, 1991; Mohajjel et al., 2003; Ghasemi and Talbot, 2006; Azizi and Moinevaziri, 2009).

All of Iran's tectonic units, including the Sanandaj-Sirjan Zone, were formed through three key processes: 1) Subduction of the Neo-Tethys oceanic crust beneath the Central Iran plate during the Lower to Upper Cretaceous. 2) Subduction of segments of the Neo-Tethys oceanic crust, such as ophiolites, along the continental margin of Central Iran during the Upper Cretaceous (Turonian to Campanian). 3) The collision between the Arabian Plate and the Central Iranian Plate during the Upper Cretaceous to the Quaternary (Alavi, 2004).

The Sanandaj-Sirjan Zone stretches approximately 1500 km from Sanandaj in the northwest to Sirjan in the southeast, with a width ranging between 150 and 200 km. This zone runs parallel to the Zagros Fold-Thrust Belt, reflecting its close tectonic and structural relationship with the broader Zagros Orogenic system (Ghazi and Moazzen, 2015). It is a prominent structural and tectonic zone in the western and central parts of Iran. The Sanandaj-Sirjan Zone (SSZ) is significant because its metamorphic, igneous, and sedimentary rocks provide evidence of complex

geological processes related to the subduction and closure of the Neo-Tethys Ocean. The SSZ is bounded to the southwest by the Zagros Fold-Thrust Belt and to the northeast by the Urumieh-Dokhtar Magmatic Arc (UDMA) (Mohajjel et al., 2003; Sepahi et al., 2018). Alavi, 1994 suggests that the Sanandaj-Sirjan Zone resulted from the opening and closing of the Neo-Tethys Ocean during the late Paleozoic and Mesozoic. Berberian and King, 1981 considered the Sanandaj-Sirjan Zone to represent an active continental margin during the Mesozoic.

The Sanandaj-Sirjan Zone primarily consists of Late Proterozoic to Mesozoic metamorphic rocks, including metacarbonates, schists, gneisses, and amphibolites. These rocks are overlain by Phanerozoic shallow-water sediments deposited on passive continental margins, and large Mesozoic gabbroic to granitic bodies have intruded into them (Ghazi and Moazzen, 2015). Additionally, Berberian and Berberian, 1981 studied the intrusive bodies in this region, which are composed of a combination of gabbro and granite. They considered these bodies to be Jurassic intrusions solely because they are overlain by Cretaceous formations.

According to the studies by Fazlnia et al., 2007, magmatic activities in the southeastern part of the Sanandaj-Sirjan Zone are attributed to tectonic processes associated with the subduction of the Neo-Tethys oceanic crust beneath central Iran. This subduction led to the formation of magma with compositions including quartz diorite, anorthosite, and apatite-pyroxenite gabbros (a mafic-ultramafic complex) in the southern part of the zone. Additionally, using the U-Pb method on zircon minerals, the age of the mafic-ultramafic body at Tale Pahlevani (Fig 2, 4. b, 4. c) was determined to be  $170.5 \pm 1.9$  Ma, while the age of the granodiorite batholith at Shahr-Babak city was determined to be  $164.3 \pm 8.1$  Ma (Jurassic).

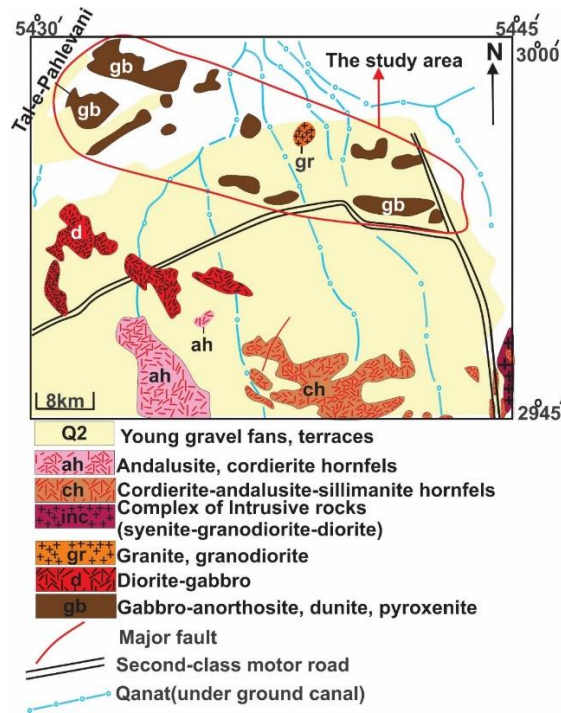


Fig 2. The location of the studied area on the 1:250000 modified geological map of Neyriz, from the Geological Survey of Iran (Valeh and Alavi Tehrani, 1985). Additionally, the positions of the gabbro bodies, arranged separately but close to each other in two rows, as well as the gabbro body of Tale Pahlevani and the granodiorite body situated between the gabbros, are shown.

The purpose of this research is to determine the tectonic-magmatic setting and the origin of the gabbroic intrusive rocks in the study area through field and laboratory work, including petrography, whole-rock chemical analysis, and the determination of the age of the last magmatic phase by U-Pb zircon geochronology. Additionally, we demonstrate the relationship between the gabbros and the granodiorite batholith of Shahr-Babak City, that these gabbro bodies are likely the precursors to the granodiorite batholith. Among the gabbro bodies, there is a granodiorite body. Based on field studies and age data, we conclude that this granodiorite body corresponds to the last and youngest magmatic phase of the Shahr-Babak City granodiorite batholith.

### Geological Background

The Sanandaj-Sirjan Zone extends from the Sabzevaran Fault in the southeast to the Turkey-Iran border in the northwest, encompassing northern Iraq (Shalair Zone) and southeastern Anatolia.

Tectonic events related to the opening and closure of the Neo-Tethys Ocean have led to the formation of diverse tectonic settings. The tectonic features of this region include ocean rifting, the development of the Neo-Tethys Ocean, subduction, and, ultimately, the closure of this oceanic basin (Fig 3).

In the Paleozoic, turbidite sediments were deposited in a turbulent setting characterized by magmatic and volcanic activities. These basins exhibited conditions similar to those of intracontinental extensional basins or incomplete rifts, which led to the formation of fractures and fissures in the crust and the development of ultrabasic rocks. During the Early Permian, this extension resulted in the opening of the Neo-Tethys Ocean, a process that continued until the end of the Middle Triassic (Fig 3. a, 3. b). During the Late Triassic to Early Jurassic, the Neo-Tethys Oceanic crust was subducted beneath the southern margin of Central Iran. This subduction led to the metamorphism of Paleozoic rocks in the region, the formation of a magmatic arc associated with the subduction, and the development of metamorphosed flysch sediments from the Jurassic-Cretaceous period, which are related to fore-arc basins (Fig 3. c). These formations are covered by carbonate sediments due to the transgression of the sea during the Early Cretaceous (Fig 3. d). Subduction continued until the Eocene, and from that time onward, as a result of continental collision, the formation of ophiolites, radiolarites, and glaucophane schists occurred (Fig 3. e). As a result of this collision, flysch basin sediments of the Tertiary containing olistolithic fragments from Cretaceous limestones, ophiolites, and some formations of the Zagros Zone were deposited over the margin of the High Zagros. The final stages of the Zagros orogeny are marked by the deposition of back-arc basin sediments and post-orogenic molasse deposits. Back-arc basin sediments, in the form of unconformities, cover the northern part of the southern Sanandaj-Sirjan Zone. Furthermore, post-orogenic molasse sediments were formed due to the erosion of the

uplifted areas resulting from the Zagros orogeny, both in the interior and along the margins of the southern Sanandaj-Sirjan Zone (Fig 3. e).

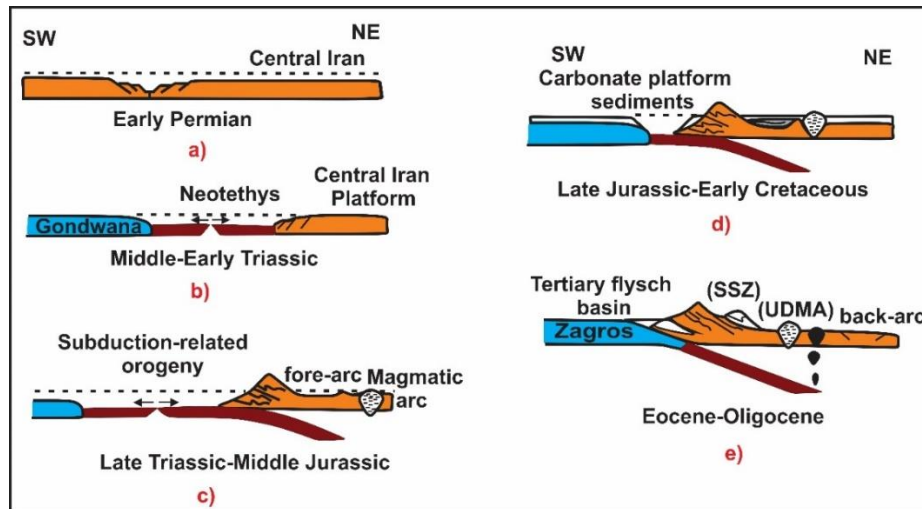


Fig 3. A simple geodynamic model of the southeastern part of the Sanandaj-Sirjan Zone illustrates the opening, expansion, and closing of the Neo-Tethys Ocean (Sheikholeslami, 2015). SSZ: Sanandaj-Sirjan Zone, UDMA: Urumieh-Dokhtar Magmatic Arc.

The fact that most of the rocks in the Sanandaj-Sirjan Zone formed during the Triassic to Jurassic periods suggests that these formations likely resulted from intense magmatic activity occurring either concurrently with or following the subduction of the Neo-Tethys Ocean. These rocks were formed beneath Central Iran during the late Triassic and early Jurassic, with magmatic activity reaching its peak in the Middle Jurassic (Aghanabati, 2004; Sheikholeslami, 2015).

### Geological Setting

Based on field observations, the Robat area includes intrusive bodies such as olivine gabbros, troctolites, dunites, and granodiorites. The gabbro bodies in this region are arranged along two trends, approximately two kilometers apart, oriented in the northwest to southeast direction. Among these gabbro bodies, a granodiorite body is exposed as an outcrop (Fig 4. a). The highest intrusive body in the region is Tale Pahlevani, which reaches an elevation of 1663 meters (Fig 4. b, 4. c). Dunite is observed in the southwest, at the contact of the Tale Pahlevani gabbro body. In

this region, dunite occurs as enclaves positioned at the upper part of the Tale Pahlevani gabbro body. These ultramafic enclaves are older than the surrounding gabbros (Fig 4. d). The olivine gabbros in the study area constitute a significant portion of the rock assemblage. In hand specimens, they are black, with a weathered surface color of dark gray. Seams and cracks are abundant in this region (Fig 4. e), and secondary calcite has infiltrated these cracks (Fig 4. f). The troctolites in the study area exhibit magmatic layering, with white layers consisting of anorthosite (Fig 4. g). The granodiorite intrusive body in this region, with an elevation of 1606 meters above sea level, outcrops along and between the gabbro bodies. Water seeps through the seams in these rocks, leading to chemical weathering in the form of onion-skin weathering (Fig 4. h).



Fig 4. a) The geological outcrop of the study area, showing the granodiorite body located between the gabbro bodies. b) General outcrop of the Tale Pahlevani gabbro body, the highest gabbro body in the region. c) Morphology of the Tale Pahlevani gabbro body. d) Ultramafic enclaves at the summit of the Tale Pahlevani gabbro body. e) Presence of contraction fractures in the olivine gabbros. f) Secondary calcite filling the cracks in the olivine gabbros. g) Magmatic layering of anorthosite in the troctolites. h) Onion-skin weathering in the granodiorites.

## Laboratory Methods

After the field studies, 70 thin sections were prepared from some collected samples, and petrographic studies were conducted using a polarizing microscope at the Shahid Bahonar University, Kerman, Iran. Subsequently, 10 samples were chosen for whole-rock chemical analysis. The details of the samples, including their geographical locations, and petrographic characteristics are provided in Table 1.

Table 1. Description of the Geographic Coordinates and Petrography of the Study Samples.

Sample	Rock Type	Geographic Coordinates (UTM)	Textures	Mineralogy (*)	
				Major minerals	Accessory minerals
RA1-A-2	Olivine gabbro	N 29°56'161 E 54°43'224	Granular Sieve Ophitic Intergranular Poikilitic Enclave	Pl: Plagioclase Afs: Alkali feldspar Ol: Olivine Cpx: Clinopyroxene	Bt: biotite Opq: Opaque Ap: Apatite
RA1-16X	Olivine gabbro	N 29°58'211 E 54°39'636	Granular Sieve Ophitic Intergranular Poikilitic Enclave	Pl: Plagioclase Afs: Alkali feldspar Ol: Olivine Cpx: Clinopyroxene	Bt: biotite Opq: Opaque Ap: Apatite
RA1-20	Olivine gabbro	N 29°58'149 E 54°39'478	Granular Sieve Ophitic Intergranular Poikilitic Enclave	Pl: Plagioclase Afs: Alkali feldspar Ol: Olivine Cpx: Clinopyroxene	Bt: biotite Opq: Opaque Ap: Apatite
RA2-16	Olivine gabbro	N 29°56'316 E 54°41'888	Granular Sieve Ophitic Intergranular Poikilitic Enclave	Pl: Plagioclase Afs: Alkali feldspar Ol: Olivine Cpx: Clinopyroxene	Bt: biotite Opq: Opaque Ap: Apatite
RA2-21	Olivine gabbro	N 29°56'424 E 54°41'615	Granular Sieve Ophitic Intergranular Poikilitic Enclave	Pl: Plagioclase Afs: Alkali feldspar Ol: Olivine Cpx: Clinopyroxene	Bt: biotite Opq: Opaque Ap: Apatite
RA2-23	Olivine gabbro	N 29°56'506 E 54°41'365	Granular Sieve Ophitic Intergranular Poikilitic Enclave	Pl: Plagioclase Afs: Alkali feldspar Ol: Olivine Cpx: Clinopyroxene	Bt: biotite Opq: Opaque Ap: Apatite

RA2-29X	Olivine gabbro	N 29°56'490 E 54°39'839	Granular Sieve Ophitic Intergranular Poikilitic Enclave	Pl: Plagioclase Afs: Alkali feldspar Ol: Olivine Cpx: Clinopyroxene	Bt: biotite Opq: Opaque Ap: Apatite
RA2-8	Troctolite	N 29°56'270 E 54°42'333	Granular Sieve Intergranular poikilitic	Pl: Plagioclase, Ol: Olivine, Cpx: Clinopyroxene	Bt: biotite Opq: Opaque Ap: Apatite
RA2-24	Dunite	N 29°56'481 E 54°39'808	Granular Mesh	Ol: Olivine Cpx: Clinopyroxene Pl: Plagioclase	Opq: Opaque Ap: Apatite
RA1-6	Granodiorite	N 29°57'741 E 54°41'127	Granular Granophyric	Pl: Plagioclase, Afs: Alkali feldspar Qz: Quartz Cpx: Clinopyroxene	Bt: biotite Opq: Opaque Ap: Apatite

(\*) Mineral abbreviations from Whitney and Evans, 2010.

Table 2. Results of geochemical analyses of major and minor element oxides in the studied samples. The analyses were conducted using X-ray Fluorescence (XRF) based on weight percentages and Laser Ablation Inductively Coupled Plasma Mass Spectrometry (LA-ICP-MS) based on ppm.

Sample	RA1-A-2	RA1-16X	RA1-20	RA2-16	RA2-21	RA2-23	RA2-29X	RA2-8	RA2-24	RA1-6
Rock Type	Olivine gabbro	Troctolite	Dunite	Granodiorite						
SiO <sub>2</sub>	45.75	45.48	46.18	43.41	45.7	45.99	45.29	45.5	39.91	63.34
Al <sub>2</sub> O <sub>3</sub>	18.21	14.44	19.59	8.88	19.65	18.59	1.96	30.9	3.1	16.43
TiO <sub>2</sub>	0.35	0.41	0.19	0.17	0.31	0.32	0.31	0.05	0.14	0.6
Fe <sub>2</sub> O <sub>3</sub>	1.85	1.91	1.69	1.67	1.81	1.82	1.81	1.55	1.64	2.1
FeO	7.9	8.48	5.57	11.59	6.39	6.6	14.26	1.12	19.05	2.99
Na <sub>2</sub> O	1.4	0.79	1	0.41	1.05	1.19	0.2	1.11	0.12	3.01
CaO	12.69	13.75	14.41	9.45	14.08	13.1	11.29	16.11	2.7	4.19
MgO	9.63	12.91	10.01	21.53	8.82	9.74	22.24	2.38	27.76	2.06
MnO	0.18	0.19	0.14	0.24	0.15	0.16	0.31	0.03	0.36	0.08
K <sub>2</sub> O	0.21	0.12	0.09	0.05	0.14	0.15	0.05	0.18	0.03	3.4
P <sub>2</sub> O <sub>5</sub>	0.02	0.03	0.02	0.02	0.03	0.04	0.02	0.02	0.03	0.19
Total	98.19	98.51	98.89	97.42	98.13	97.7	97.74	98.95	94.84	98.39
LOI	0.92	0.54	0.49	1.27	1.15	1.55	0.65	0.92	3.01	1.26
Li	14.5	11.26	7.3	8.86	9.16	14.69	15.97	10.41	14.3	32.1
Be	0.34	0.36	0.41	0.24	0.42	0.57	0.23	0.58	0.19	2.31
B	6.41	7.55	4.78	7.02	6.52	17.41	29.86	7.18	44.97	21.82
Sc	33.19	40.73	32.03	31.7	27.31	28.94	63.29	3.69	17.28	13.75
Cr	160.8	618.58	281.59	1227.08	158.57	213.67	649.87	57.7	346.63	18.79
Co	57.79	65.17	50.49	111.49	50.85	53.2	124.22	15.33	169.13	14.07
Ni	84.54	191.58	54.11	306.96	64.71	87.73	319.1	22.45	486.99	10.2
Cu	67.22	15.89	17.73	11.2	9.51	13.32	7.5	10.04	6.54	45.32
Zn	75.49	86.79	58.99	124.6	82.49	78.68	156.11	26.23	211.7	54.97
Ga	17.7	14.17	15.46	8.58	17.23	17.21	4.29	20.85	4.05	14.84
Rb	3.96	2.71	1.56	1.02	2.83	3.29	1.59	4.2	0.9	126.61
Sr	1104.32	724.67	927.86	411.24	1056.92	950.63	301.43	1621.51	133.57	498.59
Y	6.01	6.69	5.92	4.85	5.5	7.02	14.32	0.58	2.74	23.3
Zr	5.88	12.13	7.3	7.27	7.86	8.01	19.53	2.11	8.06	202.33
Nb	0.13	0.18	0.07	0.12	0.29	0.22	0.23	0.11	0.15	11.45
Mo	0.13	0.2	0.16	0.09	0.16	0.15	0.22	0.16	0.24	1
In	0.04	0	0.04	0.03	0.03	0.05	0.08	0.01	0.04	0.07
Sn	0.72	0.7	0.59	0.56	0.75	2.78	2.07	0.56	0.92	7.75
Sb	0.1	0.06	0.09	0.12	0	31.58	0.47	0.19	0.62	0.75
Cs	1.03	0.47	0.3	0.16	0.63	0.61	0.31	0.42	0.47	4.63
Ba	122.44	53.57	72.6	32.09	114.26	108.25	15.94	83.79	13.38	541.6

La	2.58	3.04	3.52	2.07	4.03	4.88	2.58	2.62	0.86	31.53
Ce	5.67	8.05	7.94	5.31	8.54	10.28	9.32	4.23	2.19	63.67
Pr	0.86	1.26	1.11	0.77	1.12	1.34	1.69	0.43	0.34	7.18
Nd	4.18	6.37	4.89	3.55	4.65	5.82	8.66	1.49	1.67	25.58
Sm	1.28	2.03	1.27	0.97	1.23	1.55	2.82	0.2	0.54	5.13
Eu	0.81	0.69	0.65	0.4	0.74	0.86	0.61	0.48	0.16	1.16
Gd	1.26	2.02	1.26	0.94	1.15	1.44	2.98	0.15	0.5	4.3
Tb	0.18	0.3	0.19	0.15	0.16	0.22	0.45	0.02	0.08	0.65
Dy	1.2	1.87	1.19	0.97	1.08	1.35	2.83	0.11	0.53	3.91
Ho	0.24	0.36	0.23	0.19	0.2	0.26	0.56	0.02	0.1	0.78
Er	0.64	0.99	0.61	0.51	0.57	0.7	1.52	0.05	0.3	2.28
Tm	0.09	0.13	0.09	0.07	0.08	0.1	0.21	0.01	0.04	0.35
Yb	0.55	0.85	0.53	0.47	0.51	0.64	1.29	0.04	0.28	2.27
Lu	0.08	0.12	0.07	0.07	0.07	0.09	0.19	0.01	0.05	0.33
Hf	0.24	0.44	0.26	0.28	0.28	0.3	0.82	0.05	0.26	4.93
Ta	0.01	0.01	0.01	0.01	0.02	0.01	0.02	0.01	0.01	0.76
W	0.68	0.12	0.16	0.3	0.12	1.04	0.26	2.04	1.8	1.1
Pb	10.6	11.33	8.05	7.78	19.9	32.79	16.37	16.25	23.41	28.2
Th	0.06	0.11	0.05	0.12	0.16	0.09	0.2	0.06	0.03	10.2
U	0.03	0.05	0.03	0.06	0.08	0.06	0.09	0.04	0.03	2.21

Chemical analyses of the major elements in these 10 rock samples were conducted using X-ray Fluorescence (XRF), while trace elements were analyzed using Laser Ablation Inductively Coupled Plasma Mass Spectrometry (LA-ICP-MS) at the University of Milan, Italy (Table 2). Samples from the study area were pulverized for whole-rock analysis using a jaw crusher, then ground into fine powder in an agate mortar, and compressed into pellets, following the procedure described by Peters and Pettke, 2017. The major, minor, and trace element compositions were analyzed using an LA-ICP-MS system, which combines a 193 nm ArF excimer laser equipped with a HelEx 2 volumetric sample chamber (Analyte Excite, Teledyne Photon Machines) and a quadrupole mass spectrometer (iCAP-Q Thermo Fisher Scientific). The BHVO basalt was analyzed alongside the unknown samples as a quality control measure (Guillong et al., 2008). In a separate experiment to determine the U-Pb age of zircon, the granodiorite body in the study area, located among the gabbros, was dated. Zircon samples for U-Pb dating were crushed using a jaw crusher and sieved to sizes ranging from 65 to 500  $\mu\text{m}$ . The zircon grains were separated by handpicking under a binocular microscope from the enriched fraction, following the standard heavy liquid separation method. All recovered zircon crystals were mounted in an epoxy resin

base, polished, and characterized by cathodoluminescence (CL) imaging. Analysis was performed using the same LA-ICP-MS instrument described above. The ablation spot was set to a diameter of 20  $\mu\text{m}$ , with a repetition rate of 10 Hz and an intensity of 2  $\text{J}/\text{cm}^2$ . Each analysis consisted of 40 seconds for background acquisition and 60 seconds for the ablation signal. The zircon reference 91500 (Wiedenbeck et al., 1995, 2004) was used as an external standard for instrument and laser corrections, including elemental fractionation. Plesovice Zircon (Sláma et al., 2008) was analyzed at each analytical step as a quality control measure. Raw data were processed using GLITTER software (Achterbergh et al., 2001). Zircons were analyzed for whole-rock analysis using the same instrument employed for LA-ICP-MS analysis (see above). Zircon trace element compositions and U-Pb geochronology were performed in two separate analytical runs. For the trace element concentration in zircon, NIST612 glass was used as the external standard and Si as the internal standard in both runs. BCR-2G glass with unknowns was analyzed as a quality control measure. The results for U-Pb zircon dating are presented in Table 3 of the supplementary material. After completing all tests, the geochemical data were processed and analyzed using graphical and specialized software (Icpet, Minpet, GCDkit), and the results were reviewed.

Table 3. Results of U-Pb zircon dating from the granodiorite sample of the Robot region, analyzed using GLITTER software.

Zircon minerals	Pb207/U235	1s	Pb206/U238	1s	rho
zrc1.1	0.0471	0.00481	0.00673	0.00014	0.20369896
zrc2.2	0.04429	0.00317	0.00648	0.00012	0.2587335
zrc3.2	0.0458	0.00353	0.00658	0.00012	0.2366171
zrc4.1	0.04539	0.0059	0.00693	0.00017	0.18872258
zrc5.1	0.04448	0.00325	0.00677	0.00012	0.24259062
zrc5.2	0.04688	0.00617	0.00674	0.00018	0.20291542
zrc9.1	0.04483	0.00482	0.00661	0.00016	0.22513355
zrc11.1	0.04466	0.00319	0.00675	0.00012	0.24888889
zrc12.1	0.04281	0.00345	0.00623	0.00012	0.23901179
zrc15.1	0.04432	0.00385	0.00689	0.00013	0.21720167
zrc15.2	0.04203	0.00345	0.00649	0.00013	0.2440276
zrc22.1	0.04393	0.00512	0.00674	0.00016	0.20368138

## Petrography

In petrographic studies, the volume percentage of minerals was used to accurately determine the names of the samples. For precise classification, IUGS classification charts from Streckeisen, 1976 were applied (Fig 5).

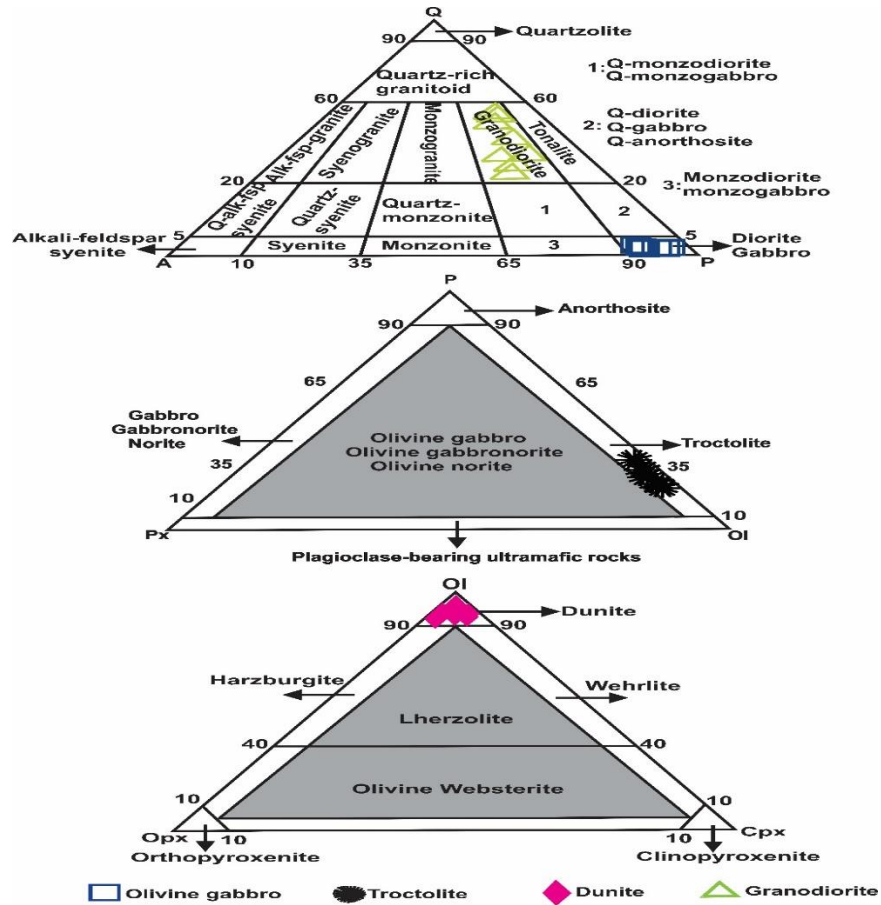


Fig 5. The location of the samples from the study area is shown in the IUGS classification diagram of Streckeisen, 1976.

Based on these studies, the samples from this region include olivine gabbros, troctolites, dunites, and granodiorites.

**Olivine gabbros:** These rocks are primarily composed of plagioclase (42%), alkali feldspar (5%), olivine (24%), and pyroxene (20%). Other minerals include opaque minerals, biotite, apatite, chlorite, calcite, and clinozoisite. Olivine gabbros display a dominant granular texture (Fig 6. a)

along with secondary textures, such as sieve texture in pyroxene (Fig 6. b), intergranular texture (Fig 6. c), ophitic texture (Fig 6. d), poikilitic texture (Fig 6. e), and magma enclaves (Fig 6. f). Additionally, zoning is observed in the plagioclase and pyroxene minerals within these rocks. In these rocks, plagioclase ranges in size from approximately 0.5 to 5 mm, with an extinction angle of 30 to 38 degrees, and is identified as labradorite. Alkali feldspars, ranging from 0.5 to 2 mm in size, and olivines, occurring in euhedral to anhedral forms and ranging from approximately 0.5 to 4.5 mm, are also present. Pyroxenes range in size from approximately 0.5 to 3 mm, have an extinction angle of 35 to 45 degrees, and are identified as clinopyroxene. Accessory minerals include opaque minerals, biotite, and apatite. Opaque minerals occur as fine grains, dispersed within other minerals and in the background. Biotite crystals are approximately 0.5 mm in size and apatite crystals measure around 0.1 mm in size. Chlorite, calcite, and clinozoisite are secondary minerals formed through the alteration of other minerals.

**Troctolites:** In these rocks (Fig 6. g), the primary minerals are plagioclase (85%), olivine (8%), and pyroxene (3%). Other minerals present in troctolites include opaque minerals, biotite, apatite, chlorite, and calcite. These rocks exhibit a dominant granular texture, along with secondary textures such as sieve, intergranular, and poikilitic. Plagioclase occurs as elongated crystals, ranging in size from 0.5 to 3.5 mm, with an extinction angle of 32 degrees, and is classified as labradorite. Olivines are euhedral to anhedral, with sizes ranging from approximately 0.5 to 2.5 mm. Pyroxenes are 0.5 mm in size, have an extinction angle of 30 degrees, and are classified as clinopyroxenes. Accessory minerals in these rocks include opaque minerals, biotite, and apatite. Opaque minerals and biotite minerals range in size from 0.5 to 1 mm. Apatites are present as very small grains within other minerals. Secondary minerals such as chlorite are found in very fine sizes, and calcite occurs as fine grains in these rocks.

**Dunites:** These rocks are primarily composed of olivine (95%), pyroxene (2%), and plagioclase (1%). Other minerals in dunites include opaque minerals, apatite, and calcite. The dominant texture of these rocks is granular (Fig 6. h). The olivine in these rocks occurs as euhedral to subhedral crystals, ranging in size from approximately 0.5 to 5 mm. The olivine minerals exhibit numerous fractures, which provide sites for the decomposition of olivine and trigger the serpentinization process along these fractures, a phenomenon known as mesh texture (Hopkinson et al., 2004) (Fig 6. h). Pyroxenes display high-series colors and have an extinction angle of 35 degrees, classifying them as clinopyroxenes. These minerals range in size from approximately 0.5 to 1.5 mm. The plagioclases range in size from 0.5 to 1.5 mm and exhibit an extinction angle of 37 degrees. They are classified as labradorite. The rocks also contain accessory minerals such as opaque minerals and apatite. Opaque minerals are present in sizes ranging from very small to 0.5 mm, embedded within other minerals. Apatite occurs as fine-grained crystals, approximately 0.1 mm in size, scattered throughout the rock matrix. The secondary mineral calcite is formed through the alteration of other minerals.

**Granodiorites:** These rocks primarily consist of plagioclase (45%), alkali feldspar (15%), quartz (20%), and pyroxene (3%). Other minerals found in granodiorites include opaque minerals, biotite, apatite, amphibole, calcite, and chlorite. The dominant texture of these rocks is granular (Fig 6. i), with a secondary granophyric texture (Fig 6. j).

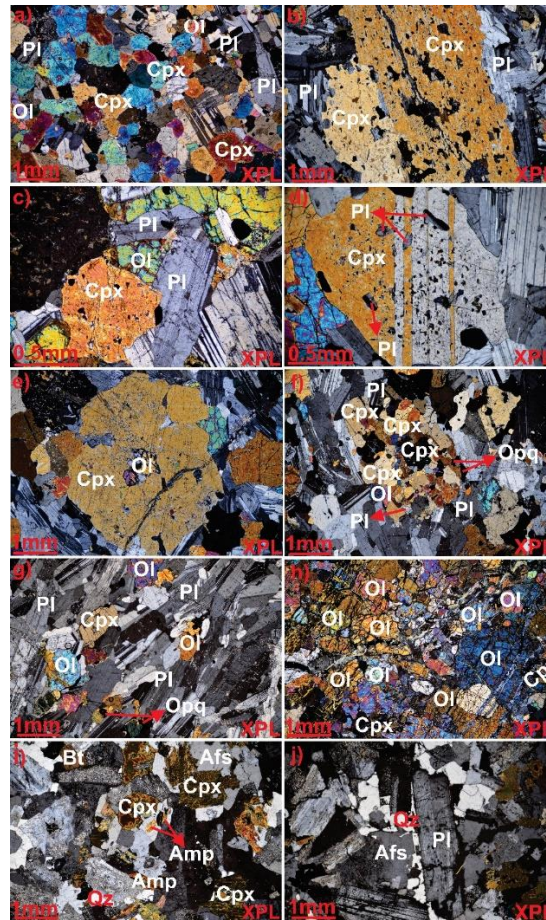


Fig 6. a) Granular texture in olivine gabbro. b) Sieve texture in pyroxene in olivine gabbro. c) Intergranular texture in olivine gabbro. d) Ophitic texture in olivine gabbro. e) Poikilitic texture in olivine gabbro. f) Magma enclave in olivine gabbro. g) Troctolite. h) Granular and mesh textures in dunite. i) Granular texture in granodiorite. j) Granophyric texture in granodiorite. Mineral abbreviations from Whitney and Evans, 2010: Pl – Plagioclase, Afs – Alkali feldspar, Cpx – Clinopyroxene, Ol – Olivine, Amp – Amphibole, Bt – Biotite, Qz – Quartz.

The plagioclase crystals in these rocks range in size from approximately 0.5 to 5 mm, with extinction angles between 30 and 38 degrees, and are classified as labradorite. Alkali feldspars range in size from approximately 0.5 to 2.5 mm, while quartz crystals, which are subhedral to anhedral with irregular margins, range in size from 0.5 to 2 mm. Pyroxenes, ranging in size from 0.5 to 2.5 mm, exhibit an extinction angle of 30 to 48 degrees and are classified as clinopyroxenes. Accessory minerals in these rocks include opaque minerals, biotite, and apatite. Biotites are light to dark brown and occur in amorphous form, with sizes ranging from 0.5 to 2.5 mm. Opaque minerals are present in sizes ranging from 0.5 to 1 mm, while apatites are very fine-grained and

occur within other minerals. Secondary minerals such as amphibole, calcite, and chlorite form due to the alteration of primary minerals. In certain areas of the rock, pyroxenes have been significantly altered and transformed into amphibole and chlorite, while plagioclase minerals have undergone metamorphic processes, leading to the formation of calcite.

## Discussion

### Whole-Rock Geochemistry

The geochemical analysis results, including Whole Rock (XRF) and LA-ICP-MS data, for the samples from the study area are presented in Table 2.

In the  $\text{Na}_2\text{O}+\text{K}_2\text{O}$  versus  $\text{SiO}_2$  classification diagram (after Middlemost, 1994), the samples from this region are located in the gabbro and peridotite gabbro and belong to the sub-alkaline magmatic series (Fig 7. a). In the AFM diagram (after Irvine and Baragar, 1971), the olivine gabbros and dunites from this region are classified as tholeiitic, while the troctolites and granodiorites are associated with the calc-alkaline series (Fig 7. b).

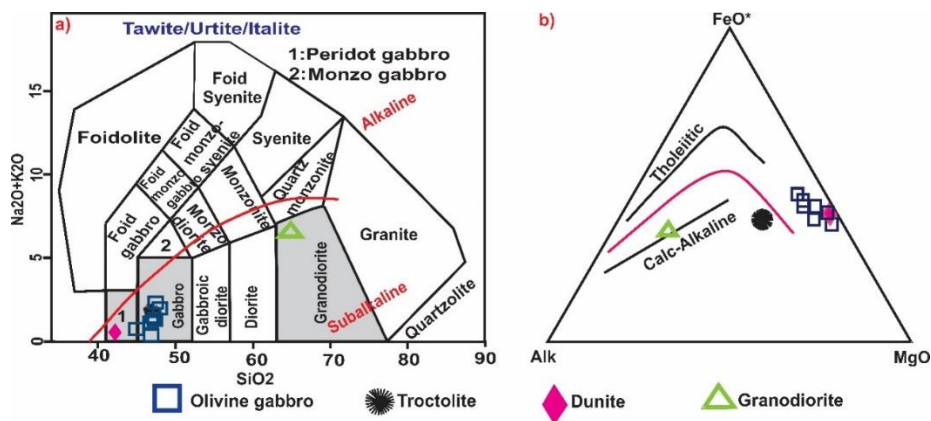


Fig 7. a) Location of the samples from the studied area in the  $\text{Na}_2\text{O}+\text{K}_2\text{O}$  versus  $\text{SiO}_2$  (TAS) classification diagram (after Middlemost, 1994). b) Position of the samples from the studied area in the AFM diagram (after Irvine and Baragar, 1971).

In the normalized plot of element concentrations relative to chondrite composition (Boynton, 1984), the olivine gabbro and troctolite samples from the studied area exhibit a positive Eu anomaly (Fig 8. a), which is more pronounced in the troctolite samples. This positive Eu anomaly may be attributed to the accumulation of plagioclase (Jagoutz and Kelemen, 2015). In the olivine gabbros and dunites of the studied area, no negative Yb anomaly is observed, suggesting that the magma originated from a spinel-lherzolite mantle source (Ali et al., 2022). However, in the troctolites from this region, a negative Yb anomaly is present. This anomaly cannot be solely attributed to the presence of garnet in the source but may instead result from the mixing of melts derived from both spinel-lherzolite and garnet-lherzolite mantle sources (Ali et al., 2022).

In the normalized spider diagram of element concentrations relative to the primary mantle composition (Sun and McDonough, 1989), the samples from the studied area exhibit a positive anomaly for elements such as Cs, Ba, U, K, Pb, Sr, Nd, Sm, and Eu, and a negative anomaly for elements including Rb, Th, Nb, P, Zr, and Ti (Fig 8. b).

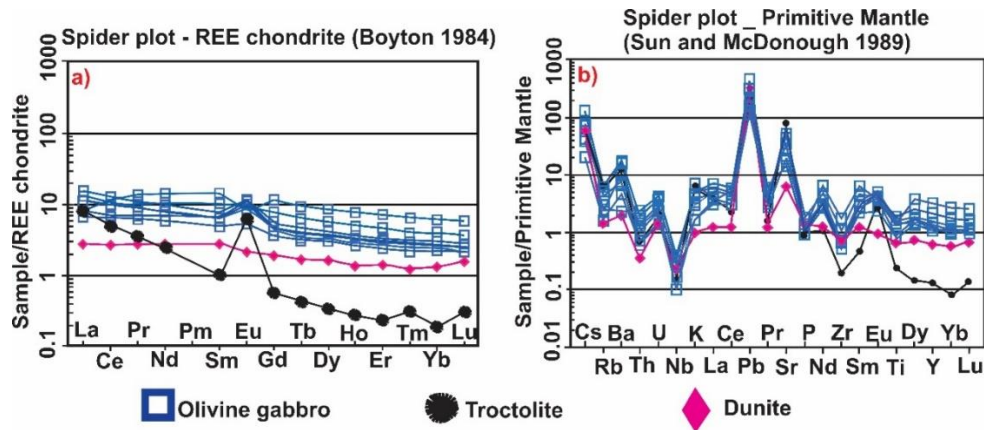


Fig 8. a) The location of the samples from the studied area in the normalized spider diagram of element concentrations relative to chondrite composition (Boynton, 1984). b) The location of the samples from the studied area in the normalized spider diagram of element concentrations relative to primary mantle composition (Sun and McDonough, 1989).

The enrichment of Ba is attributed to the high proportion of amphibole minerals in the samples, and the positive anomalies of Ba and K suggest that the magmas are associated with subduction processes (Fazlnia and Alizadeh, 2013). A positive anomaly in Sr reflects the abundance of plagioclase minerals, while a negative anomaly in Zr is associated with the fractional crystallization of clinopyroxenes (Fall et al., 2023). The enrichment of U points to the addition of altered oceanic crust or pelagic sediments to the parental magma of the rock samples (Fan et al., 2003). The enrichment of Nd is attributed to its relatively small atomic number and large ionic radius compared to other elements in the REE group, allowing it to preferentially accumulate in minerals such as titanite and apatite. Additionally, the enrichment of rare earth elements (REE) in the samples from the studied area may result from the concentration of these elements during the final stages of fractional crystallization (Srivastava and Singh, 2004). The positive anomalies of Ba, Sr, and Sm suggest a metasomatized mantle source (Zhao and Zhou, 2007; Fazlnia and Alizadeh, 2013). The enrichment of Ba and the depletion of Nb and Ti in the samples from this region can be attributed to several factors, including: 1) the formation of the samples in subduction zones, 2) contamination of the samples by the upper crust (Shang et al., 2004). The depletion of the P element in the samples from the studied area suggests its incorporation into the apatite mineral (Espinoza et al., 2008).

## **Magmatic Evolution**

Based on field observations, ultramafic enclaves are present within the gabbroic rocks of the study area, which are attributed to fractional crystallization processes (Zhang and Szilas, 2024). In the troctolitic samples, anorthosites with a completely white color are observed as part of magmatic layering. This layering is commonly seen as alternating dark and light bands, which might have formed due to fractional processes (Shelley, 1993). Furthermore, the gabbroic body in this region

exhibits onion-skin weathering, likely caused by the considerable age of the gabbros and the relatively high humidity of the area.

Petrographic studies at the microscopic scale reveal various textures in the rock samples, formed under the influence of different factors. For instance, granular texture indicates the depth of crystallization, typically associated with bodies that have cooled slowly at significant depths within the Earth's crust. Crystal formation is governed by three processes: nucleation, diffusion, and growth. Each of these processes operates at different rates depending on the prevailing conditions (Shelley, 1993). The intergranular texture is a common texture in gabbroic rocks, where smaller minerals, such as pyroxene, olivine, or iron-titanium oxides, occupy the spaces between larger plagioclase crystals (Homam, 2017). The ophitic texture forms due to the simultaneous crystallization of plagioclase and pyroxene minerals. In other words, the arrangement of fine plagioclase crystals within pyroxene results from differences in nucleation and growth rates. Minerals like pyroxene do not readily nucleate but grow easily, forming large crystals. In contrast, when nucleation occurs more readily, smaller and more numerous minerals are formed. As a result, plagioclase crystals within pyroxene tend to remain small and are unable to grow significantly (McKenzie and Nions, 1998). In other words, the ophitic texture results from the higher nucleation rate of plagioclase minerals compared to the lower nucleation rate and higher growth rate of pyroxene minerals (Vernon, 2018). The poikilitic texture forms when minerals grow to enclose other minerals, reflecting the crystallization process in igneous rocks (Shelley, 1993). Sieve textures and enclaves develop as a result of the initial crystallization of magma (Chatterjee et al., 2021). These textures indicate disequilibrium conditions during magma solidification (Filipov and Janasi, 2008).

In the dunites of the study area, two types of textures are observed: granular and mesh. In these rocks, olivine minerals exhibit fractures that act as a medium for the initiation of the serpentinization process. This process begins at these fractures and leads to the formation of the mesh texture. The mesh texture is one of the pseudomorphic textures of serpentine, where olivine minerals are transformed into serpentine due to the infiltration of water, fluids, and the presence of silica and magnesium. The serpentinization reaction typically starts at the fractures in the olivine crystals and, as hydration progresses, extends inward toward the crystal core (Hopkinson et al., 2004). However, when hydration levels are low, olivine does not fully transform into serpentine (Deer et al., 2013). Similar conditions have been observed in the dunites of this region. This process, driven by hydrothermal solutions, follows the chemical reaction below (Deer et al., 2013):



In the granodiorites of this region, a granophyric texture is present, formed by the simultaneous crystallization of quartz and alkali feldspar during the final stages of intercrystalline melt (Skursch et al., 2024).

To investigate the magmatic changes, plots of the oxide variations of major elements against MgO (Fig 9) were used. In all the plots, the samples from the study area are dispersed, which is attributed to their coarse-grained nature. As MgO increases, the Al<sub>2</sub>O<sub>3</sub> oxide shows a decreasing trend from troctolite to olivine gabbro, and finally to dunite (Fig 9. a). The decrease in Al<sub>2</sub>O<sub>3</sub> against MgO in gabbroic rocks is attributed to fractional crystallization. As gabbroic magma cools and crystallizes, minerals such as olivine and pyroxene, which are rich in MgO, crystallize, depleting the remaining melt of MgO. The crystallization of plagioclase and feldspar further enriches the residual melt in Al<sub>2</sub>O<sub>3</sub> (Abdullah, 2019). As MgO increases, the amount of FeO oxide increases from troctolite to olivine gabbro, and finally to dunite (Fig 9. b).

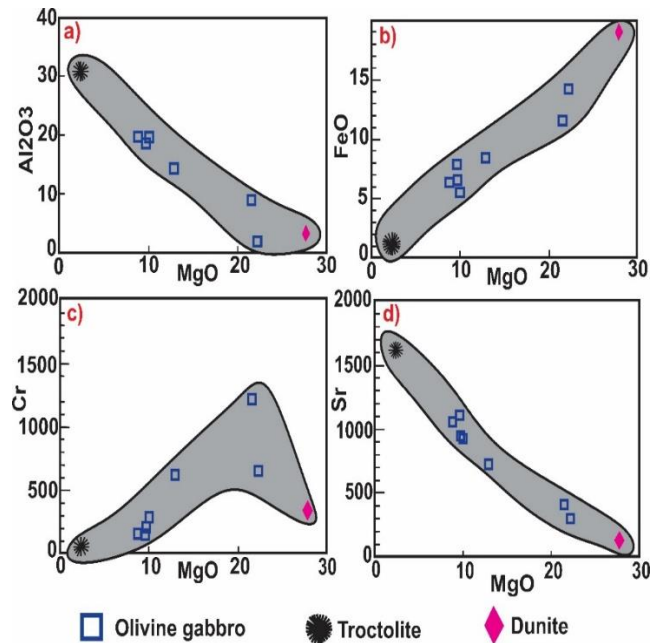


Fig 9. a, b) The positions of the samples from the study area in the graphs showing the variations of some oxides of major elements against MgO. c, d) The graphs depicting the variations of some trace elements against MgO.

The increase in FeO relative to MgO in gabbroic rocks is primarily controlled by fractional crystallization, oxygen fugacity conditions, the composition of the primary magma, and interactions between crystallized minerals (Khalil et al., 2023).

In the plot of Cr versus MgO, as the MgO content increases, the concentration of chromium rises from the troctolite samples towards dunite, followed by olivine gabbro (Fig 9. c). Chromium is compatible with primary crystallized minerals such as clinopyroxene, and as MgO increases, chromium also increases due to the fractional crystallization of Cr-bearing phases (Wang et al., 2019). In the Sr versus MgO plot, a downward trend is observed from troctolite to olivine gabbro and finally to dunite (Fig 9. d). The decrease in Sr with increasing MgO in gabbroic rocks can be explained by the fractional crystallization of plagioclase during magma solidification. As the magma cools, plagioclase, which incorporates Sr into its crystal structure, begins to crystallize,

removing Sr from the remaining liquid. This leads to a decrease in Sr concentration, as MgO is also reduced in the residual melt, which eventually forms gabbroic rocks (Hayes et al., 2024).

Based on the Nb/U versus La/Sm diagram from Krienitz et al., 2006, the samples from this region plot within the field of the upper continental crust (Fig 10. a). Crustal materials are typically depleted in Nb and enriched in light rare earth elements (LREE). The low Nb/U ratio in the rock samples, compared to mantle compositions, suggests that the magmas that formed these rocks underwent crustal contamination. In the samples from the study area, this ratio is 4.8, indicating the involvement of crustal contamination.

The Rb/Y versus Nb/Rb diagram from Temel et al., 1998 is used to distinguish between fluid-induced enrichment in subduction zones, crustal contamination, and intra-plate enrichment. In this diagram, the samples from the study area sequentially trend from olivine gabbros and dunites to granodiorites and troctolites, towards the subduction zone or crustal contamination field (Fig 10. b).

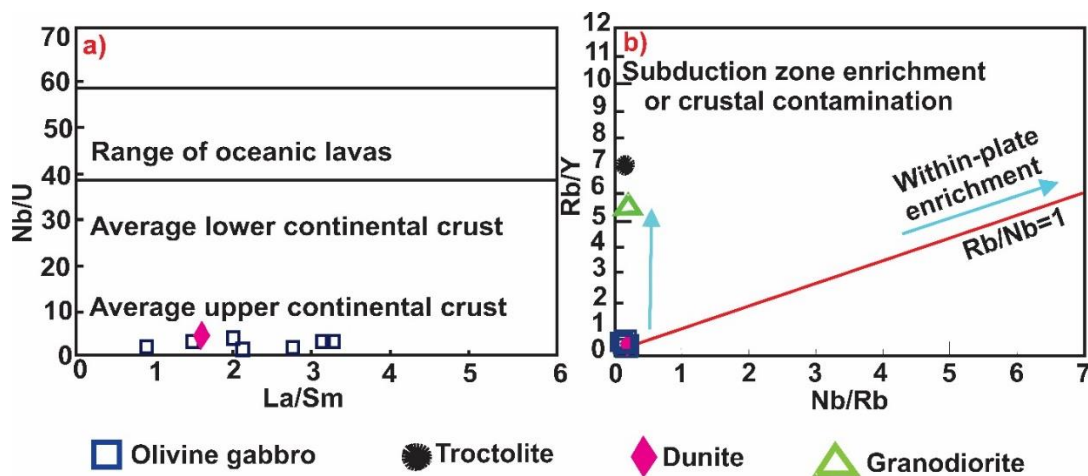


Fig 10. a) The position of the study area in the Nb/U versus La/Sm diagram from Krienitz et al., 2006 is shown. b) The position of the study area in the Rb/Y versus Nb/Rb diagram from Temel et al., 1998 is shown.

## Geochronology

In this study, U-Pb dating was performed on zircon minerals from the granodiorites of the study area, with the results presented in Table 3. The age of the granodiorite body in the region is  $42.65 \pm 0.49$  Ma (Eocene) (Fig. 11).

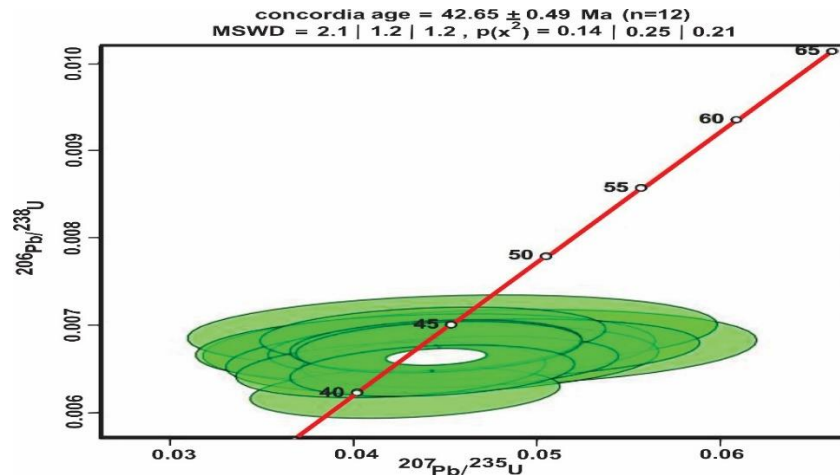


Fig. 11. Concordia diagram for the granodiorites of the Robat region based on zircon U-Pb data.

This granodiorite body, which outcrops along and between the gabbro bodies, represents the youngest magmatic phase in the area.

## Petrogenesis

Gabbroic rocks predominantly form in specific geological environments characterized by the slow cooling of mafic magma beneath the Earth's surface. The key geological settings where gabbroic rocks occur are as follows: **1- Mid-Ocean Ridges:** Gabbros are commonly derived from the crystallization of mid-ocean ridge basalts (MORB). These melts accumulate in magma chambers, where they cool gradually, resulting in the formation of gabbroic bodies (Tribuzio et al., 2004). **2- Ophiolite Complexes:** Gabbros constitute a significant component of ophiolite complexes, which represent sections of oceanic crust that have been uplifted and exposed on land. These complexes frequently include layered gabbros as a characteristic feature (Follmann et al., 2021). **3-**

**Subduction Zones and Continental Arcs:** Gabbroic rocks are also associated with subduction-related processes and continental volcanism. They form beneath volcanic arcs and in settings of alkaline volcanic activity (Khezerlou et al., 2020).

Based on the Th/Ta versus Yb diagram (Schandl and Gorton, 2002), the samples from the study area are positioned in the active continental margin domain (Fig 12. a). Similarly, the Th/Nb versus La/Yb diagram (Hollocher et al., 2012) places the samples within the continental arc domain (Fig 12. b). In the Nb/Zr versus Zr diagram (Thieblemont and Tegye, 1994), the samples from the study area are located within the subduction zone field (Fig 12. c). Furthermore, the Ce/Yb versus Sm/Yb diagram (Fleche et al., 1998) indicates that a depth of 65 km marks the boundary between the garnet-lherzolite and spinel-lherzolite mantle. The samples, ranging from dunite to olivine gabbro, are inferred to have originated from depths of 60 to 65 km. This suggests that the parental volcanic magma of the samples was derived from an enriched spinel-lherzolite mantle (Fig 12. d).

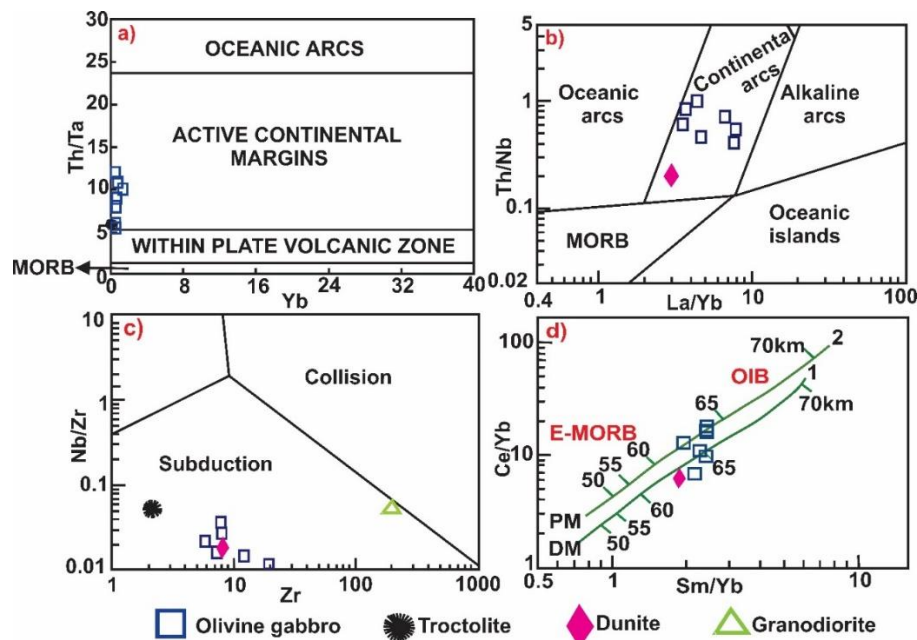


Fig 12. Locations of samples from the study area are depicted in the following diagrams: a) Th/Ta versus Yb diagram (Schandl and Gorton, 2002). b) Th/Nb versus La/Yb variation diagram (Hollocher et al., 2012). c) Nb/Zr versus Zr variation diagram (Thieblemont and Tegye, 1994). d) Ce/Yb versus Sm/Yb variation diagram (Fleche et al., 1998).

## Conclusion

Based on field investigations conducted in the region and the findings of this study, the gabbros in the studied area are likely precursors to the Shahr-Babak granodiorite intrusion. The key evidence supporting this hypothesis includes the following: 1- The gabbros are linear in distribution and occur along the margins of the granodiorites. 2- Anorthosites injected into the fractures and seams of the gabbros are genetically linked to the granodiorites. 3- No granodiorite enclaves are observed within the gabbros. 4- The gabbros, with an age of  $170.5 \pm 1.9$  Ma, are older than the Shahr-Babak granodiorite batholith, dated at  $164.3 \pm 8.1$  Ma. Additionally, the granodiorite body exposed between the northern gabbro outcrop walls has an age of  $42.65 \pm 0.49$  Ma, marking the youngest and final magmatic phase in the region.

In petrographic studies and at the microscopic scale, disequilibrium textures such as sieve textures and zoning are observed in the plagioclase and pyroxene minerals of the samples from this region. These textures are formed due to the presence of hydrous minerals in these rocks and are the result of changes in water fugacity during magma crystallization.

In the geochemical investigations of whole rock, the samples from the studied area are classified as gabbro and peridotite-gabbro and are sub-alkaline in terms of their magmatic series. The olivine gabbros and dunites of the region are tholeiitic, while the troctolites and granodiorites are calc-alkaline.

In the normalized diagram of element concentrations relative to chondrite composition, the troctolite samples from the studied area prominently exhibit a positive Eu anomaly and a negative Yb anomaly. The positive Eu anomaly may be due to the accumulation of plagioclase, while the negative Yb anomaly is not specifically related to the presence of garnet in the source region. It

could instead result from the mixing of melts from both the spinel-lherzolite and garnet-lherzolite mantle sources. In the normalized spider diagram of element concentrations relative to the composition of the primary mantle for the samples from this region, positive anomalies of elements such as Cs, Ba, U, K, Pb, Sr, Nd, Sm, and Eu, as well as negative anomalies of elements such as Rb, Th, Nb, P, Zr, and Ti, are observed. Overall, the chondrite-normalized spider diagram indicates that factors such as crustal contamination, fractional crystallization, and processes related to subduction play a role in the geochemical variations of the samples from this region.

In tectonic setting studies, the samples from this region are located at the active continental margin and are associated with an arc-continent position. They have undergone contamination by upper continental crust materials. These samples are linked to subduction processes, with their parental magmatic compositions originating from a depleted spinel-lherzolite mantle.

## **Acknowledgments**

I would like to express my gratitude to Dr. Marco Filippi for his training on the laboratory equipment, Dr. Gianluca Sessa and Mr. Andrea Risplendente, the laboratory technicians, and all members of the Department of Earth Sciences at the University of Milan (Italy). I also thank the Ministry of Science, Research, and Technology of Iran for providing the study opportunity scholarship, as well as the Shahid Bahonar University of Kerman (Iran). Additionally, I sincerely appreciate the editor and reviewers of *Periodico di Mineralogia* for their valuable feedback and insightful comments, which greatly contributed to improving the quality of this manuscript.

## References

- Abdullah P., 2019. Geology and petrography of gabbroic rocks from Khanozai Ophiolite, Northwestern Pakistan. *International Research Journal of Earth Sciences* 7 (3).
- Achterbergh V. E., Ryan C. G., Jackson S. E., Griffin W. L., 2001. Data reduction software for LA-ICP-MS: appendix. *Laser Ablation-ICP-Mass Spectrometry in the Earth Sciences: Principles and Applications*, 239-243.
- Aghanabati S. A., 2004. Geology of Iran (In Persian). *Geological Survey of Iran Publications*.
- Alavi M., 1991. Sedimentary and structural characteristics of the Paleo-Tethys remnants in northeastern Iran. *Geological Society of America Bulletin*, 103(8), 983-992.
- Alavi M., 1994. Tectonics of the Zagros orogenic belt of Iran: new data and interpretations. *Tectonophysics*, 229 (3-4), 211-238.
- Alavi M., 2004. Regional stratigraphy of the Zagros fold-thrust belt of Iran and its proforeland evolution. *American journal of Science*, 304(1), 1-20.
- Ali S., Abart R., Sayyed M. I., Hauzenberger C. A., Sami M., 2022. Petrogenesis of the Wadi El-Faliq Gabbroic Intrusion in the Central Eastern Desert of Egypt: Implications for Neoproterozoic post-collisional magmatism associated with the Najd fault system. *Minerals*, 13(1), 10.
- Azizi H. and Moinevaziri H., 2009. Review of the tectonic setting of Cretaceous to Quaternary volcanism in northwestern Iran. *Journal of Geodynamics*, 47(4), 167-179.
- Berberian F. and Berberian M. J. Z. H. K. H. G. E., 1981. Tectono-plutonic episodes in Iran. *Zagros Hindu Kush Himalaya Geodynamic Evolution*, 3, 5-32.
- Berberian M. and King G. C. P., 1981. Towards a paleogeography and tectonic evolution of Iran. *Canadian journal of earth sciences*, 18(2), 210-265.
- Boynton W. V., 1984. Cosmochemistry of the rare earth elements: meteorite studies. In *Developments in Geochemistry*. Elsevier (Vol. 2), 63-114.

- Chatterjee S., Bandyopadhyay D., Takazawa E., Michibayashi K., 2021. Orthopyroxene–magnetite symplectite in olivine gabbros from the lower crustal Oman Ophiolite: Oman Drilling Project, Hole GT2A. *Journal of Mineralogical and Petrological Sciences*, 116(3), 170-175.
- Deer W. A., Howie R. A., Zussman J., 2013. *An introduction to the rock-forming minerals*. Mineralogical Society of Great Britain and Ireland, 510 p.
- Espinoza F., Morata D., Polvé M., Lagabrielle Y., Maury R. C., Guivel C., ... Suárez M., 2008. Bimodal back-arc alkaline magmatism after ridge subduction: Pliocene felsic rocks from Central Patagonia (47 S). *Lithos*, 101(3-4), 191-217.
- Fall M., Labou I., Ndiaye P. M., 2023. Petrography, Geochemistry and Relative Chronology of Quaternary Volcanic Formations in the Mermoz and Fann Sectors, West Senegal. *International Journal of Geosciences*, 14(8), 733-766.
- Fan W. M., Gue F., Wang Y. J., Lin G., 2003. Late Mesozoic calc-alkaline volcanism of post-orogenic extension in the northern Da Hinggan Mountains, northeastern China. *Journal of volcanology and geothermal research*, 121: 115-135.
- Fazlnia A.N., Moradian A., Rezaei K., Moazen M., ALI P. S., 2007. Synchronous activity of anorthositic and S-type granitic magmas in Chah-Dozdan batholith, Neyriz, Iran: evidence of zircon SHRIMP and monazite CHIME dating.
- Fazlnia A. and Alizade A., 2013. Petrology and geochemistry of the Mamakan gabbroic intrusions, Urumieh (Urmia), Iran: magmatic development of an intra-oceanic arc. *Periodico di Mineralogia*, 82(2), 263-290.
- Filipov M. and de Assis Janasi V., 2008. The Mauá granitic massif, Central Ribeira Belt, São Paulo: petrography geochemistry and U-Pb dating. *Brazilian Journal of Geology*, 31(3), 341-348.
- Fleche M. R., Camiré G., Jenner G. A., 1998. Geochemistry of post-Acadian, Carboniferous continental intraplate basalts from the Maritimes Basin, Magdalen islands, Quebec, Canada. *Chemical Geology*, 148(3-4), 115-136.
- Follmann J., Van der Zwan F. M., Preine J., Hübscher C., Bousquet R., Augustin N., 2021. Gabbro discovery in discovery deep: first plutonic rock samples from the Red Sea rift axis. *Frontiers in Earth Science*, 9, 742815.

- Ghasemi A. and Talbot C. J., 2006. A new tectonic scenario for the Sanandaj–Sirjan Zone (Iran). *Journal of Asian Earth Sciences*, 26(6), 683-693.
- Ghazi J. M. and Moazzen M., 2015. Geodynamic evolution of the Sanandaj-Sirjan zone, Zagros orogen, Iran. *Turkish Journal of Earth Sciences*, 24(5), 513-528.
- Guillong M., Meier D. L., Allan M. M., Heinrich C. A., Yardley B. W., 2008. Appendix A6: SILLS: A MATLAB-based program for the reduction of laser ablation ICP-MS data of homogeneous materials and inclusions. *Mineralogical Association of Canada Short Course*, 40, 328-333.
- Hayes B., Ashwal L. D., Khumalo K. B., Iaccheri L. M., 2024. Major, trace element and Sr-Nd isotope evidence for a sublithospheric mantle source for the Umkondo large igneous province. *Geoscience Frontiers*, 15(1), 101719.
- Hollocher K., Robinson P., Walsh E., Roberts D., 2012. Geochemistry of amphibolite-facies volcanics and gabbros of the Støren Nappe in extensions west and southwest of Trondheim, Western Gneiss Region, Norway: a key to correlations and paleotectonic settings. *American Journal of Science*, 312(4), 357-416.
- Homam M., 2017. *Igneous Petrology*. (In Persian). 4th Edition, Ferdowsi University of Mashhad Press, 180.
- Hopkinson L., Beard J. S., Boulter C. A., 2004. The hydrothermal plumbing of a serpentinite-hosted detachment: evidence from the West Iberia non-volcanic rifted continental margin. *Marine Geology*, 204(3-4), 301-315.
- Irvine T. N. and Baragar W. R. A., 1971. A guide to the chemical classification of the common volcanic rocks. *Canadian journal of earth sciences*, 8(5), 523-548.
- Jagoutz O. and Kelemen P. B., 2015. Role of arc processes in the formation of continental crust. *Annual Review of Earth and Planetary Sciences*, 43(1), 363-404.
- Khalil K., Summers P., El-Shazly A., 2023. Origin of the post-collisional younger gabbroic rocks and the associated Fe–Ti oxide ores, Abu Ghalaga area, Southern Eastern Desert, Egypt: mineralogical and geochemical constraints. *Arabian Journal of Geosciences*, 16(3), 160.
- Khezerlou A. A., Grégoire M., Amel N., Moayyed M., Jahangiri A., Kilzi M., 2020. Origin and formation process of Gabbro and Diorite Xenoliths in the northern part of Uromieh-Dokhtar Magmatic Belt, NW Iran: constraints from mineral and whole-rock chemistries. *The Journal of Geology*, 128(2), 227-246.

- Krienitz M. S., Haase K. M., Mezger K., Eckardt V., Shaikh-Mashail M. A., 2006. Magma genesis and crustal contamination of continental intraplate lavas in northwestern Syria. *Contributions to Mineralogy and Petrology*, 151, 698-716.
- McKenzie D. and O'Nions R. K., 1998. Melt production beneath oceanic islands. *Physics of the Earth and Planetary Interiors*, 107(1-3), 143-182.
- Middlemost E. A., 1994. Naming materials in the magma/igneous rock system. *Earth-science reviews*, 37(3-4), 215-224.
- Mohajjel M., Fergusson C. L., Sahandi M. R., 2003. Cretaceous-Tertiary convergence and continental collision, Sanandaj–Sirjan zone, western Iran. *Journal of Asian Earth Sciences*, 21(4), 397-412.
- Morley C. K., Kongwung B., Julapour A. A., Abdolghafourian M., Hajian M., Waples D., Kazemi H., 2009. Structural development of a major late Cenozoic basin and transpressional belt in central Iran: The Central Basin in the Qom-Saveh area. *Geosphere*, 5(4), 325-362.
- Peters D. and Pettke T., 2017. Evaluation of major to ultra trace element bulk rock chemical analysis of nanoparticulate pressed powder pellets by LA-ICP-MS. *Geostandards and Geoanalytical Research*, 41(1), 5-28.
- Schandl E. S. and Gorton M. P., 2002. Application of high field strength elements to discriminate tectonic settings in VMS environments. *Economic geology*, 97(3), 629-642.
- Sepahi A. A., Salami S., Lentz D., McFarlane C., Maanijou M., 2018. Petrography, geochemistry, and U–Pb geochronology of pegmatites and aplites associated with the Alvand intrusive complex in the Hamedan region, Sanandaj–Sirjan zone, Zagros orogen (Iran). *International Journal of Earth Sciences*, 107, 1059-1096.
- Sheikholeslami M. R., 2015. Tectonostratigraphic units of the southeastern part of the Sanandaj–Sirjan Zone. *Scientific Quarterly Journal of Geosciences*, 24(95), 243-253.
- Shang G. K., Satir M., Sieble W., Nasifa E. N., Taubuld H., Liegeoise J. P., Tchoua F. M., 2004. Geochemistry, Rb–Sr and Sm–Nd systematic: case of the Sangmelima region, Ntem complex, southern Cameroon. *Journal of African Earth Sciences*, 40(1-2), 61-79.

- Shelley D., 1993. Igneous and metamorphic rocks under the microscope: classification, textures, microstructures, and mineral preferred orientations. (No Title).
- Skursch O., Tegner C., Barfod G. H., Andreasen R., Leshner C. E., 2024. Granites and Granophyres of the Bushveld Complex, South Africa: A review. *Earth-Science Reviews*, 104703.
- Srivastava R. K. and Singh R. K., 2004. Trace element geochemistry and genesis of Precambrian sub-alkaline mafic dikes from the central Indian craton: evidence for mantle metasomatism. *Journal of Asian Earth Sciences*, 23(3), 373-389.
- Sláma J., Košler J., Condon D. J., Crowley J. L., Gerdes A., Hancher J. M., Whitehouse M. J., 2008. Plešovice zircon—a new natural reference material for U–Pb and Hf isotopic microanalysis. *Chemical Geology*, 249(1-2), 1-35.
- Streckeisen A., 1976. To each plutonic rock its proper name. *Earth-science reviews*, 12(1) 1-33.
- Sun S. S. and McDonough W. F., 1989. Chemical and isotopic systematics of oceanic basalts: implications for mantle composition and processes. Geological Society, London, Special Publications, 42(1), 313-345.
- Temel A., Gündoğdu M. N., Gourgaud A., 1998. Petrological and geochemical characteristics of Cenozoic high-K calc-alkaline volcanism in Konya, Central Anatolia, Turkey. *Journal of volcanology and geothermal research*, 85(1-4), 327-354.
- Thieblemont D. and Tegye M., 1994. Geochemical discrimination of differentiated magmatic rocks attesting for the variable origin and tectonic setting of calc-alkaline magmas. *Comptes Rendus De L Academie des Sciences Serie II*, 319(1), 87-94.
- Tribuzio R., Thirlwall M. F., Vannucci R., 2004. Origin of the gabbro–peridotite association from the Northern Apennine Ophiolites (Italy). *Journal of Petrology*, 45(6), 1109-1124.
- Valeh N. and Alavi Tehrani N., 1985. Geological Survey of Iran. 1:250000 Neyriz Scale Map.
- Vernon R. H., 2018. A practical guide to rock microstructure. Cambridge university press.

- Wang J., Wang X., Liu J., Liu Z., Zhai D., Wang Y., 2019. Geology, geochemistry, and geochronology of gabbro from the Haoyaoerhudong gold deposit, Northern Margin of the North China Craton. *Minerals*, 9(1), 63.
- Whitney D. L. and Evans B. W., 2010. Abbreviations for names of rock-forming minerals. *American mineralogist*, 95(1), 185-187.
- Wiedenbeck M. A. P. C., Alle P., Corfu F. Y., Griffin W. L., Meier M., Oberli F. V., Spiegel W., 1995. Three natural zircon standards for U-Th-Pb, Lu-Hf, trace element and REE analyses. *Geostandards newsletter*, 19(1), 1-23.
- Wiedenbeck M., Hanchar J. M., Peck W. H., Sylvester P., Valley J., Whitehouse M., Zheng Y. F., 2004. Further characterisation of the 91500 Zircon crystal. *Geostandards and Geoanalytical Research*, 28(1), 9-39.
- Zhang L. and Szilas K., 2024. Eoarchean ultramafic rocks represent crustal cumulates: A case study of the Narssaq ultramafic body, southern West Greenland. *Earth and Planetary Science Letters*, 625, 118508.
- Zhao J. H. and Zhou M. F., 2007. Geochemistry of Neoproterozoic mafic intrusions in the Panzihua district (Sichuan Province, SW China): Implications for subduction-related metasomatism in the upper mantle. *Precambrian research*, 152(1-2), 27-47.